# RESEARCH ARTICLE

## Scale-by-scale energy budget in fractal element grid-generated turbulence

R. Jason Hearst and Philippe Lavoie*

*Institute for Aerospace Studies, University of Toronto, Toronto, M3H 5T6, Canada*

(*Received 00 Month 200x; final version received 00 Month 200x*)

Measurements were conducted downstream of a square-fractal-element grid at $Re_{L_0} = UL_0/\nu = 65,000$, where $L_0$ is the size of the largest element in the grid. The scale-by-scale energy budget for grid turbulence is used to investigate the phenomenological change in the turbulence between the inhomogeneous and homogeneous regions downstream of the grid, providing greater insight into the evolution of the turbulence in these two regions. It is shown that in the far-field, $x/L_0 \geq 20$, where the flow is approximately homogeneous and isotropic, the scale-by-scale energy budget proposed by Danaila et al. [1] for grid turbulence is well balanced. In the near-field, $x/L_0 < 20$, the same energy budget is not satisfied, with the imbalance of the budget occurring at scales in the range $\lambda \lesssim r \lesssim L_0$. It is proposed that the imbalance is caused by non-zero transverse transport of turbulent kinetic energy and production due to transverse mean velocity gradients. Approach of the spectra to $k^{-5/3}$ behaviour with a decade long scaling range in the inhomogeneous region is attributed to forcing by these non-zero transverse terms.

**Keywords:** grid turbulence, homogeneous turbulence, isotropic turbulence, energy budget, fractal grid

## 1. Introduction

Kolmogorov [2, 3] developed a relationship between the second- and third-moments of the longitudinal velocity increments over a spatial interval $r$. These moments are typically referred to as the second- and third-order structure functions, represented by $\langle(\delta u)^2\rangle$ and $\langle(\delta u)^3\rangle$, respectively, where $u$ is the turbulent fluctuation in the $x$-direction, $\delta u = u(x+r) - u(x)$ and $\langle\cdot\rangle$ is an ensemble average in the homogeneous directions. The relationship developed by Kolmogorov is given by

$$-\langle(\delta u)^3\rangle + 6\nu\frac{\mathrm{d}}{\mathrm{d}r}\langle(\delta u)^2\rangle = \frac{4}{5}\langle\epsilon\rangle\, r, \qquad (1)$$

where $\langle\epsilon\rangle$ is the mean turbulent kinetic energy dissipation rate. Equation (1) can be thought of as a scale-by-scale energy budget with respect to the energy contained at a scale $r$. The first term on the left-hand-side of (1), which is the third moment of velocity, represents the energy transferred through advection. The second term, which includes the rate of change of the second moment of velocity, represents the energy transferred through molecular diffusion. The derivation of (1) assumes a cascade of energy and sufficiently high Reynolds numbers such that the small scales are locally isotropic and adequately separated from the large scales to be uninfluenced by them.

---

*Corresponding author. Email: lavoie@utias.utoronto.ca

2    *Taylor & Francis and I.T. Consultant*

Grid turbulence and turbulent jet measurements found that (1) was not satisfied at the large scales [1, 4–6]. Consequently, Danaila et al. [1] derived the following relationship for homogeneous, locally isotropic grid turbulence:

$$-\langle(\delta u)(\delta q)^2\rangle + 2\nu\frac{\mathrm{d}}{\mathrm{d}r}\langle(\delta q)^2\rangle - \frac{U}{r^2}\int_0^r s\frac{\partial}{\partial x}\langle(\delta q)^2\rangle\,\mathrm{d}s = \frac{4}{3}\langle\epsilon\rangle\,r, \tag{2}$$

where $\langle(\delta q)^2\rangle = \langle(\delta u)^2\rangle + \langle(\delta v)^2\rangle + \langle(\delta w)^2\rangle$, $\langle(\delta u)(\delta q)^2\rangle = \langle(\delta u)^3\rangle + \langle(\delta u)(\delta v)^2\rangle + \langle(\delta u)(\delta w)^2\rangle$, and $s$ is a dummy integration variable. Equation (2) may be represented simply as $G + D + I = C$. $G$ and $D$ are analogous to the first two terms of (1). However, $I$ has been added to account for the influence of longitudinal inhomogeneity resulting from the decay of turbulence behind the grid. Furthermore, (2) is more robust than (1) because it was derived under the assumption of local, rather than global, isotropy. All four terms of (2) may be measured experimentally, and as such it is common to refer to the 'balance' of the energy budget to describe how well the measured left-hand-side approximates the measured right-hand-side of (2). The balance, $B^*$, may be explicitly defined as $G/C + D/C + I/C = G^* + D^* + I^* = B^*$, where $B^* = 1$ represents the case where (2) is fully satisfied. Lavoie et al. [7] found that if grid turbulence measurements are performed with adequate longitudinal spatial resolution such that the $I$ term is resolved (measurements typically need to be performed with spacings on the order of the grid mesh length, $M$), then $B^* = 1$ at all $r$ to within $\pm 5\%$.

Accurately determining the gradient term in the integral of $I$ may not always be feasible due to the requirement of relatively fine spacing in $x$ measurements. In such cases, the similarity form of (2), derived by Antonia et al. [8] and based on the work of George [9], may provide an alternative means of estimating the scale-by-scale energy budget without the necessity of detailed $x$ measurements. The similarity form of (2) is given by [8]

$$g(\tilde{r}) + 2\frac{\mathrm{d}f(\tilde{r})}{\mathrm{d}\tilde{r}} - \left[\frac{5\Gamma_1(\tilde{r})}{n} - 10\Gamma_2(\tilde{r})\right]\frac{1}{\tilde{r}^2} = \frac{20}{3}\tilde{r}, \tag{3}$$

where $n$ is the exponent of the power-law decay of turbulent kinetic energy $\langle q^2\rangle \sim (x - x_0)^n$, and a tilde denotes normalization by the Taylor microscale whose square is given by

$$\lambda^2 = 5\nu\frac{\langle q^2\rangle}{\langle\epsilon\rangle}, \tag{4}$$

where $\langle q^2\rangle = \langle u^2\rangle + \langle v^2\rangle + \langle w^2\rangle$. The functions in (3) are given by [8]

$$g(\tilde{r}) = -\langle(\delta u)(\delta q)^2\rangle\left(\frac{3^{1/2}Re_\lambda}{\langle q^2\rangle^{3/2}}\right), \tag{5a}$$

$$f(\tilde{r}) = \frac{\langle(\delta q)^2\rangle}{\langle q^2\rangle}, \tag{5b}$$

$$\Gamma_1(\tilde{r}) = \int_0^{\tilde{r}} \tilde{s}^3 f'\,\mathrm{d}\tilde{s}, \tag{5c}$$

$$\Gamma_2(\tilde{r}) = \int_0^{\tilde{r}} \tilde{s}^2 f \, \mathrm{d}\tilde{s}, \tag{5d}$$

where $\tilde{s} = s/\lambda$ is a dummy integration variable and the Taylor microscale Reynolds number is

$$Re_\lambda = \frac{\langle q^2 \rangle^{1/2} \lambda}{3^{1/2} \nu}. \tag{6}$$

Similar to (2), (3) may be written as $G_s + D_s + I_s = C_s$. It then follows that the balance of the similarity form of the scale-by-scale energy budget is given by $B_s^* = G_s/C_s + D_s/C_s + I_s/C_s = G_s^* + D_s^* + I_s^*$. This similarity analysis has been shown to be approximately satisfied in grid turbulence in multiple studies [7, 10, 11].

Recent experiments by Vassilicos and co-workers with space-filling square-fractals have rekindled interest in grid-generated turbulence [12–15]. The space-filling square-fractal grids are a single fractal that occupies the entire wind tunnel cross-section. These grids have produced results that contrast with those of classical grid-generated turbulence. For instance, space-filling square fractals have been shown to produce turbulence that decays according to a power-law with $n \approx -2.5$, which represents very rapid decay relative to classical grids and theoretical expectations where $-1 \leq n \leq -1.4$ [14]. Turbulent spectra with scaling ranges that exist over a decade have also been observed, which are atypical of classical grids (the lack of a scaling range for classical grid turbulence is typically attributed to insufficient $Re_\lambda$). Furthermore, although the core of the flow has been reported as approximately homogeneous [12–14], non-zero transverse transport of turbulent kinetic energy has been measured [14]. These studies were conducted in the range $x/L_0 < 20$, where $L_0$ is the largest element length in the grid geometry.

Krogstad and Davidson [16, 17] have extensively investigated the near- and far-field of multi-scale cross-grids and found that the flow is highly inhomogeneous near the grid and decays with an accelerated rate relative to the far-field where the flow is homogeneous and decays with an exponent near $n = -1.2$. If one assumes that $L_0$ from a square fractal is equivalent to $M$ for a cross-grid or classical grid, then the investigation area of earlier square fractal studies is very close to the grid where one might expect inhomogeneity. Furthermore, Valente and Vassilicos [14] specifically argue that the range of scales induced by a cross-grid may not be sufficient to produce the same results as a square fractal geometry. Hence, while the near- and far-fields of classical and cross-grid geometries are reasonably well understood, the same is not true for square fractal grids.

The above was the basis for the work of Hearst and Lavoie [18] who designed a square-fractal-element grid featuring a $12 \times 8$ arrangement of small fractal elements mounted to a background mesh (see Figure 1). Measuring in the range $3.5 \leq x/L_0 \leq 48.5$, Hearst and Lavoie [18] showed that the atypical results associated with previous fractal studies were related to the proximity of the measurements to the grid itself. They showed that for the region $x/L_0 < 20$ the flow was inhomogeneous and exhibited the same properties as previous fractal studies, while in the region $x/L_0 \geq 20$ the flow was approximately homogeneous and reached a state that agreed well with classical Richardson-Kolmogorov phenomenology, including a decay exponent of $n = -1.37$.

The present study employs the same square-fractal-element grid to investigate the phenomenological differences between the near-grid, $x/L_0 < 20$, and the far-field, $x/L_0 \geq 20$, regions of fractal-generated turbulence in order to determine the
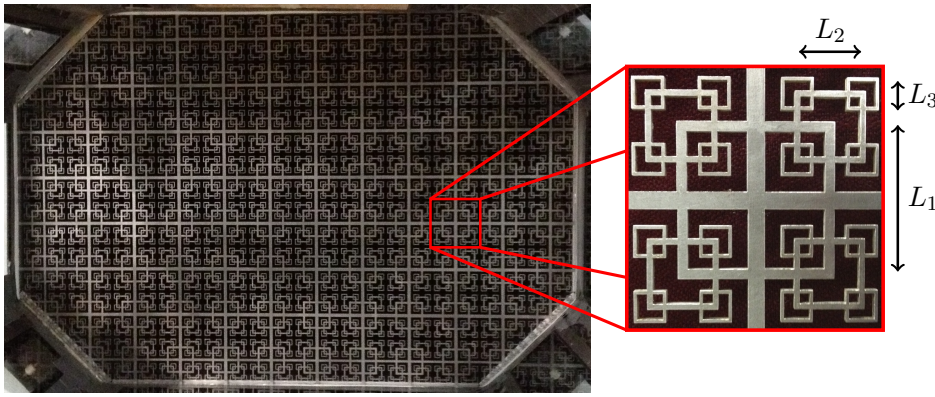
Figure 1.  Square-fractal-element grid positioned *in situ* (left) with a magnified view of a single fractal element (right) and primary grid dimensions.

sources of near-field inhomogeneity and if high-order statistics in the far-field agree with predictions for homogeneous, isotropic turbulence (HIT). While Hearst and Lavoie [18] investigated transverse profiles of the mean velocity and turbulence intensity, the present study considers the scale-by-scale energy budget, transverse transport of turbulent kinetic energy, and production as metrics for the approximation of HIT by the square-fractal-element flow. The primary aim of the present work is thus to further reconcile fractal-generated and classical grid-generated turbulence measurements.

## 2.    Experimental setup

The grid was laser-cut from a single piece of 3 mm thick stainless steel. The geometry consists of a $12 \times 8$ matrix of square fractal elements with $N = 3$ fractal iterations. The lengths of the fractal iterations are $L_i = 55.6$ mm, 24.7 mm, and 11.0 mm where $L_{i+1} = L_i/R_L$ with $R_L = 2.25$, and the thicknesses are $t_i = 4.1$ mm, 2.5 mm, and 1.5 mm, where $t_{i+1} = t_i/R_t$ with $R_t = 1.65$. The background mesh has dimensions of $L_0 = 100$ mm and $t_0 = 6.7$ mm. The grid solidity is $\sigma = 0.39$.

The study was conducted in a low-speed wind tunnel with dimensions 5.0 m $\times$ 1.2 m $\times$ 0.8 m (length $\times$ width $\times$ height); the background turbulence intensity was $\sim 0.05\%$. Measurements were acquired at $Re_{L_0} = UL_0/\nu = 65{,}000$ with a X-wire, using a Dantec 56C-series anemometer. The hot-wire probes were prepared in-house using Dantec prongs and 2.5 $\mu$m thick copper-coated tungsten wire. Wire sensing lengths were maintained at $\ell = 0.55 \pm 0.05$ mm, ensuring the required length-to-diameter ratio of 200. This resulted in spatial resolutions ranging $1.4 \leq \ell/\eta \leq 5.6$ dependent on $x$, where $\eta = \nu^{3/4}/\langle\epsilon\rangle^{1/4}$ is the Kolmogorov microscale. Streamwise measurements were performed over the range $3.5 \leq x/L_0 \leq 48.5$ in $x/L_0 = 0.35$ increments. Measurements were made slightly off-centre, $(y, z) = (30 \text{ mm}, 0)$, as it was found that this produced the best approximation of $U \sim$ constant $(\pm 1\%)$ along the test-section length. Transverse scans at $x/L_0 = 10$, 25, 35, and 45 were also conducted in the range $-2.6 \leq y/L_0 \leq 2.1$ in increments of $y/L_0 = 0.3$. All measurements were acquired for 8 minutes or longer, ensuring better than $\pm 1\%$ convergence of $\langle q^2 \rangle$, estimated from $\langle q^2 \rangle \approx \langle u^2 \rangle + 2\langle v^2 \rangle$, and $\pm 5\%$ convergence of the peak of $\langle(\delta u)(\delta q)^2\rangle$, estimated from $\langle(\delta u)(\delta q)^2\rangle = \langle(\delta u)^3\rangle + 2\langle(\delta u)(\delta v)^2\rangle$, using the 95% confidence interval [19]. Post-acquisition, the data were recursively low-pass filtered with a fifth-order digital Butterworth filter at the Kolmogorov frequency, $f_K = U/2\pi\eta$, using the technique described in [20]. Corrections were

applied for the finite spatial resolution of the hot-wire probes and the inherent filtering effects of numerical differentiation using a Wyngaard-style approach [21–24]. The methodology employed for post-processing, including a discussion of the assumptions needed, is given by Hearst and Lavoie [18]. For the majority of the measurements, the applied corrections were less than 1% for $\langle u^2 \rangle$ and $\langle v^2 \rangle$, and less than 5% for $\langle (\partial u / \partial x)^2 \rangle$ and $\langle (\partial v / \partial x)^2 \rangle$, with corrections for the gradients approaching 10% near the grid.

The mean turbulent kinetic energy dissipation rate, $\langle \epsilon \rangle$, hereafter referred to simply as dissipation, is estimated in the present study via two means. In the far-field, $x/L_0 \geq 20$, where the flow was approximately homogeneous and isotropic, the dissipation is given by

$$\langle \epsilon \rangle_d = -\frac{U}{2} \frac{\partial \langle q^2 \rangle}{\partial x}. \tag{7}$$

Equation (7) is derived from the turbulent kinetic energy budget for HIT, and thus is only valid for flows that approximate HIT. Estimates of $\langle \epsilon \rangle_d$ are made using a power-law fit to $\langle q^2 \rangle$ in order to reduce the effect of noise associated with discrete spatial differentiation of $\langle q^2 \rangle$. The power-law fit reported in [18] is $\langle q^2 \rangle = 14.35(x/L_0 - 7.0)^{-1.37}$, applying from $23.8 \leq x/L_0 \leq 48.5$. In the inhomogeneous near-grid region, $x/L_0 < 20$, dissipation is estimated from

$$\langle \epsilon \rangle_{XW} = 3\nu \left[ \left\langle \left( \frac{\partial u}{\partial x} \right)^2 \right\rangle + 2 \left\langle \left( \frac{\partial v}{\partial x} \right)^2 \right\rangle \right]. \tag{8}$$

The estimates of $\langle \epsilon \rangle_d$ and $\langle \epsilon \rangle_{XW}$ agree to within $\pm 8\%$ in the far-field.

## 3.    Scale-by-scale energy budget for grid turbulence

The scale-by-scale energy budget for the turbulence produced by the square-fractal-element grid is investigated in the context of the normalized version of (2), i.e. $G^* + D^* + I^* = B^*$, which are functions of $\tilde{r} = r/\lambda$. The assumptions of (2) are less restrictive than (3), hence whenever the gradient of $I$ may be evaluated accurately, (2) is preferred. The $\partial \langle (\delta q)^2 \rangle / \partial x$ term of $I$ was calculated by fitting sixth-order polynomials to $\langle (\delta q)^2 \rangle$ along $x$ for each $r$ over the ranges $3.5 \leq x/L_0 \leq 34.0$ and $17.9 \leq x/L_0 \leq 48.5$, and taking $\partial/\partial x$ analytically. This technique is similar to that employed in [7], where a single polynomial was used. Two overlapping polynomials were used in the present study given the significant differences in homogeneity and energy decay identified by Hearst and Lavoie [18] in the near- and far-fields. In the region where the two polynomials overlap, a linear weighting was used between them to average the resulting gradient curves. Although data was acquired over the range $3.5 \leq x/L_0 \leq 48.5$, the scale-by-scale budget was only investigated for $5 \leq x/L_0 \leq 45$ in order to reduce the influence of end effects.

Figure 2 shows the normalized scale-by-scale energy budget at three locations in the grid far-field and demonstrates that (2) is balanced to within 10% there. Thus, (2) adequately represents the far-field turbulence. The location of the peak of $G^*$ at $\tilde{r} \approx 1$ is also in good agreement with previous grid turbulence measurements [7, 11] and analytical models [10]. Furthermore, the individual terms are nearly equal given the current normalization, which implies that they are self-similar to a good approximation. This result is consistent with previous grid measurements that have found this scaling to be approximately satisfied [11, 25].
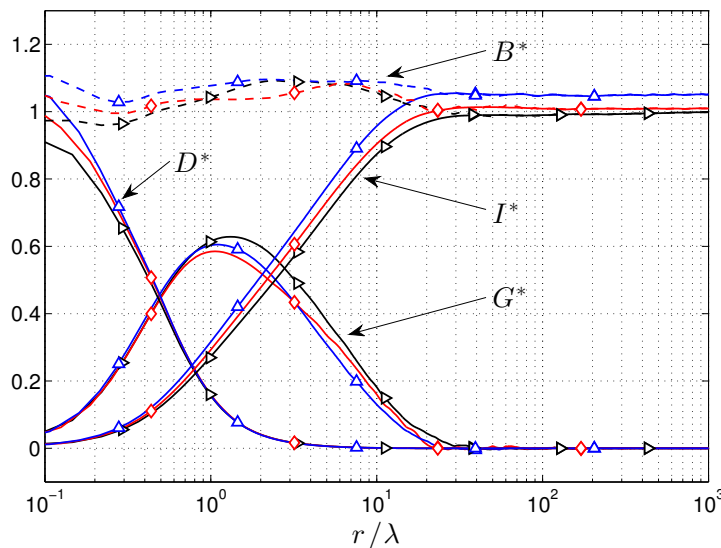
Figure 2.   Normalized terms of the scale-by-scale energy budget for grid-turbulence, given by (2), at three locations in the far-field; ($\triangleright$) $x/L_0 = 27.3$, $Re_\lambda = 83$; ($\diamond$) $x/L_0 = 34.7$, $Re_\lambda = 80$; ($\triangle$) $x/L_0 = 42.4$, $Re_\lambda = 80$.

Figure 3 shows the terms of (2) for three locations in the near-grid region. The present dataset allows a unique perspective on the scale-by-scale energy budget, as the measurements are performed such that $\langle (\delta u)(\delta q)^2 \rangle$ is resolved at every measurement station. As such, contours of $B^*$ are plotted in Figure 4. From Figures 3 and 4, where there are peaks in $B^*$ exceeding 30% of unity, it is clear that the balance of (2) is significantly better for $x/L_0 \geq 20$ compared to $x/L_0 < 20$. This corresponds to the homogeneous and inhomogeneous regions of the flow. As such, Figure 4 explicitly illustrates the phenomenological difference in the near- and far-field flows. Furthermore, the strong imbalance for $x/L_0 < 20$ is located between the peak of $G^*$ and the plateau of the inhomogeneous term, $I^*$, typically in the range $1 \lesssim \tilde{r} \lesssim 40$. Interestingly, the return to $B^* = 1$ appears to always be at scales near the size of $L_0$ (represented by a dashed line in Figure 4), hence the imbalance is approximately restricted to $\lambda < r < L_0$. Recall that the growth of $\lambda$ in grid turbulence can be significant as it can be shown that $\lambda^2 \sim (x - x_0)$, which is approximately true for the present grid [18]. As such, $L_0/\lambda$ decreases with $x/L_0$.

In order to determine if the chosen streamwise axis accurately reflects the flow field as a whole, the transverse hot-wire scans at $x/L_0 = 10$, 25, 35 and 45 were investigated in the context of the similarity form of the scale-by-scale energy budget given by (3). Similarity must be invoked to evaluate the scale-by-scale budget across the transverse scans because there is insufficient streamwise data to accurately estimate the gradient term of $I$ off the primary axis. Figure 5 shows the normalized terms of the similarity form of the scale-by-scale energy budget given by (3) at $y/L_0 = -1.0$, 0, and 1.3, which are representative of all $y/L_0$, for the aforementioned streamwise positions. Variations with $y/L_0$ are only present for the nearest measurement location ($x/L_0 = 10$), suggesting that the choice of the transverse location does not affect the results of the scale-by-scale budget for $x/L_0 \geq 25$. $B_s^*$ is also comparable in the far-field to the results for $B^*$. Figure 5 thus confirms that the far-field results in Figures 2 and 4 are representative of the entire HIT far-field flow. In the near-field, the exact magnitude by which $B_s^*$ deviates from unity is dependent on $y/L_0$, but the imbalance occurs at several $y/L_0$ and is a distinguishing feature compared to the far-field measurements.

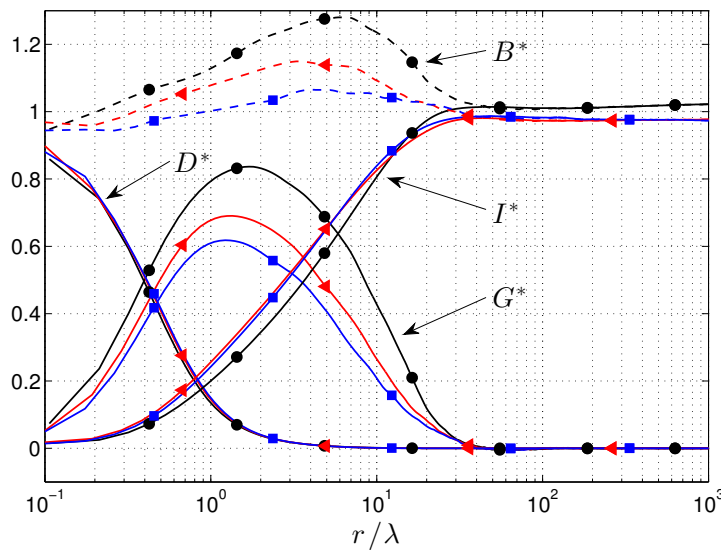Comparing experimental and DNS measurements of decaying and forced turbu-

Figure 3.   Normalized terms of the scale-by-scale energy budget for grid-turbulence, given by (2), at three locations in the near-field; (●) $x/L_0 = 10.2$, $Re_\lambda = 138$; (◄) $x/L_0 = 15.8$, $Re_\lambda = 106$; (■) $x/L_0 = 20.0$, $Re_\lambda = 93$.
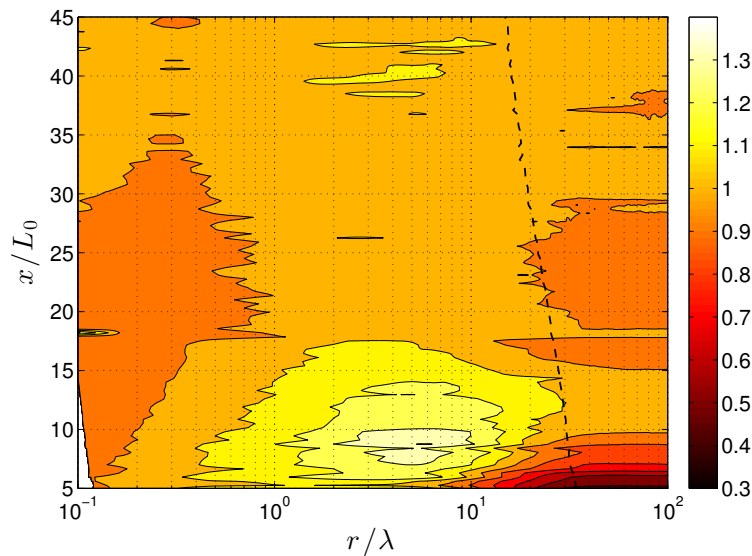


Figure 4.   Contour plot of the the balance of the scale-by scale energy budget, $B^* = G^* + D^* + I^*$, which is equal to unity when (2) is fully satisfied. The *dashed line* represents $L_0/\lambda$.

lence, Antonia and Burattini [10] identified that for a given $Re_\lambda$, forced turbulence causes both a growth in the peak of $\langle(\delta u)^3\rangle$, the isotropic analogue of $\langle(\delta u)(\delta q)^2\rangle$, and in the location of its peak relative to decaying turbulence. In a jet flow, Rajagopalan et al. [26] investigated how a disk mesh that partially obstructs the core of a jet nozzle influenced the energy budget. They found that the disk mesh excited the shear layer, effectively injecting energy into the flow. These authors measured both growth of $G^*$ and movement of its peak to higher $r$ values relative to the case without the disk mesh. Figure 6 shows contours of $G^*$ from the present data with the locations of the peak values marked. The figure demonstrates that for $x/L_0 < 20$, $G^*$ has a broad peak that occurs at $\tilde{r} > 1$. However, as $x/L_0$ grows, the shape of $G^*$ collapses to within $\pm 4\%$ with a relatively constant peak at $\tilde{r} \approx 1.1$. This suggests that the near-grid region of a fractal wake includes appreciable energy
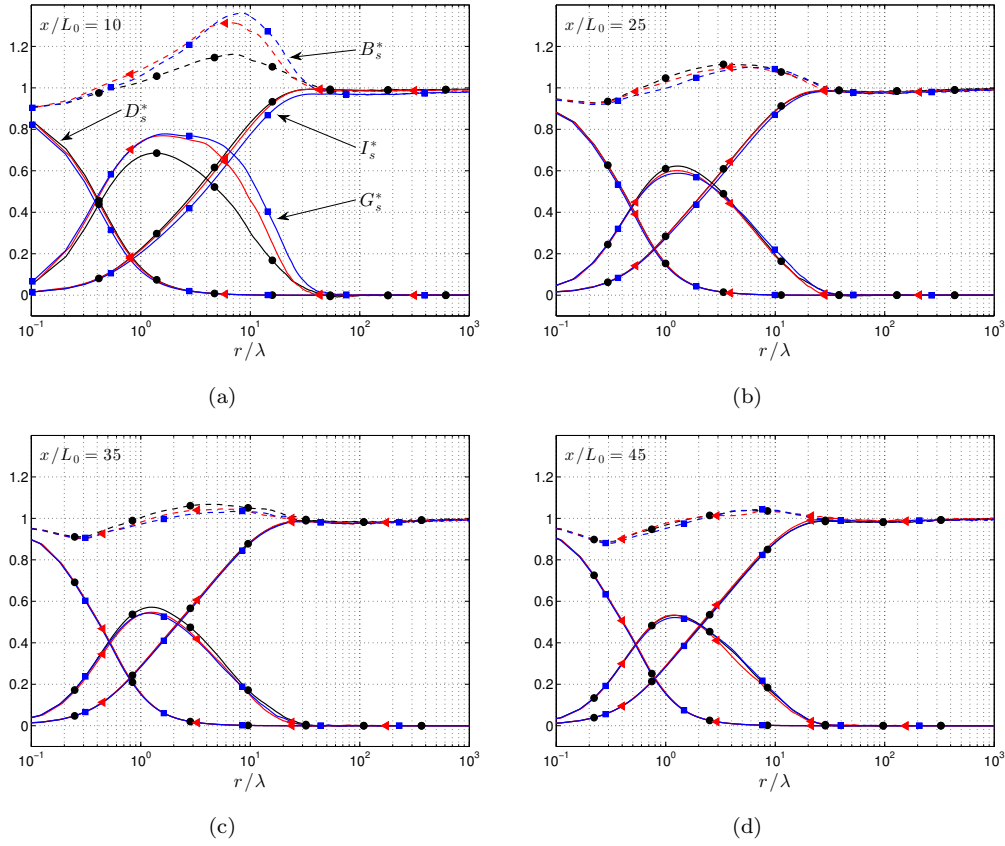
Figure 5.   Normalized terms of the similarity form of the scale-by-scale energy budget for grid-turbulence, given by (3), at three transverse locations for each streamwise location; ($\bullet$) $y/L_0 = 1.3$; ($\blacktriangleleft$) $y/L_0 = 0.0$; ($\blacksquare$) $y/L_0 = -1.0$.

injection or forcing.

## 4.   Production and transverse transport of energy

Hearst and Lavoie [18] observed mean shear in the region $x/L_0 < 20$ behind the square-fractal-element grid, which suggests that there may be production there. In the same region relative to $L_0$, Valente and Vassilicos [14] observed that there was non-zero transverse transport of turbulent kinetic energy behind a space-filling square fractal grid. These phenomena are addressed here in the context of the turbulent kinetic energy equation [27]:

$$\frac{U_k}{2}\frac{\partial \langle q^2 \rangle}{\partial x_k} = -\langle u_i u_j \rangle \frac{\partial U_i}{\partial x_j} - \frac{\partial}{\partial x_k}\left(\frac{\langle u_k q^2 \rangle}{2} + \frac{\langle u_k p \rangle}{\rho}\right) + \frac{\nu}{2}\frac{\partial^2 \langle q^2 \rangle}{\partial x_m \partial x_m} - \langle \epsilon \rangle, \quad (9)$$

where Einstein's summation notation is used. Along the centreline of grid-generated turbulence, Valente and Vassilicos [14] simplified (9) to:

$$\frac{U}{2}\frac{\partial \langle q^2 \rangle}{\partial x} = -\left(\langle u^2 \rangle \frac{\partial U}{\partial x} + 2\langle uv \rangle \frac{\partial U}{\partial y}\right) - \left(\frac{\partial}{\partial x}\frac{\langle uq^2 \rangle}{2} + 2\frac{\partial}{\partial y}\frac{\langle vq^2 \rangle}{2}\right)$$
$$- \left(\frac{\partial}{\partial x}\frac{\langle up \rangle}{\rho} + 2\frac{\partial}{\partial y}\frac{\langle vp \rangle}{\rho}\right) + \frac{\nu}{2}\left(\frac{\partial^2 \langle q^2 \rangle}{\partial x^2} + 2\frac{\partial^2 \langle q^2 \rangle}{\partial y^2}\right) - \langle \epsilon \rangle, \quad (10)$$
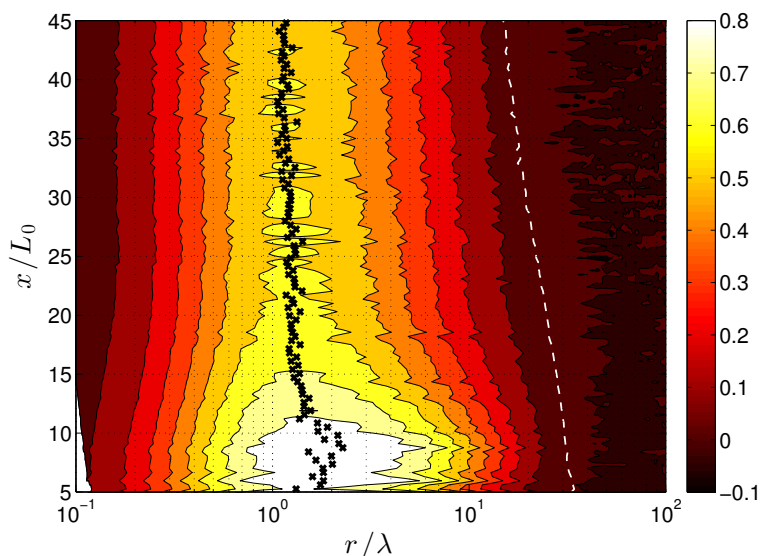
Figure 6.   Contour plot of $G^* = -\langle(\delta u)(\delta q)^2\rangle/(4/3\langle\epsilon^2\rangle r)$; ($\times$) mark the peak of $G^*$ at each $x/L_0$, and the *dashed line* represents $L_0/\lambda$.
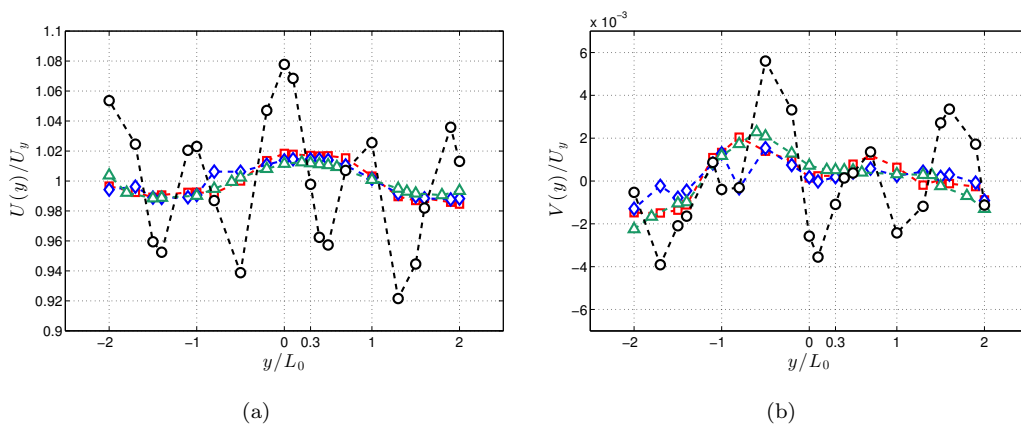


(a)                                              (b)

Figure 7.   Transverse profiles of the normalized mean velocities, $U$ and $V$; ($\bigcirc$) $x/L_0 = 10$, ($\square$) $x/L_0 = 25$, ($\Diamond$) $x/L_0 = 35$, ($\triangle$) $x/L_0 = 45$.

where the first four bracketed terms on the right-hand-side represent, respectively, production, triple-correlation transport, pressure transport, and viscous diffusion. If these four terms are zero, (10) simplifies to (7).

The presence of mean shear for $x/L_0 < 20$ as identified by Hearst and Lavoie [18], is investigated here in the context of sources causing $B^* \neq 1$. Figure 7 shows transverse profiles of both $U$ and $V$. The mean of $U(y)$ in each transverse plane, $\langle U(y)\rangle = U_y$, is used for normalization. Figure 7(a) demonstrates that there is mean shear in the near-grid area, which diminishes, i.e. $\partial U/\partial y \to 0$, as $x/L_0$ grows. Figure 7(b) also shows that the transverse gradient of the transverse velocity is non-zero, i.e. $\partial V/\partial y \neq 0$, near the grid. The homogeneity of both $U$ and $V$ improves with the downstream evolution of the turbulence and as $B^* \to 1$ for all $\tilde{r}$.

The relevant term of (9) to assess the influence of non-zero transverse gradients is the production term, $\langle u_i u_j\rangle (\partial U_i/\partial x_j)$. The experiment is designed such that $\partial U/\partial x \approx 0$, and hence there is no significant contribution to production from this term. The two transverse terms which may be measured are $\langle uv\rangle (\partial U/\partial y)$ and $\langle v^2\rangle (\partial V/\partial y)$, both of which are shown normalized by dissipation in Figure 8. The dissipation used to normalize the production is $\langle\epsilon\rangle_y$, the mean of the transverse
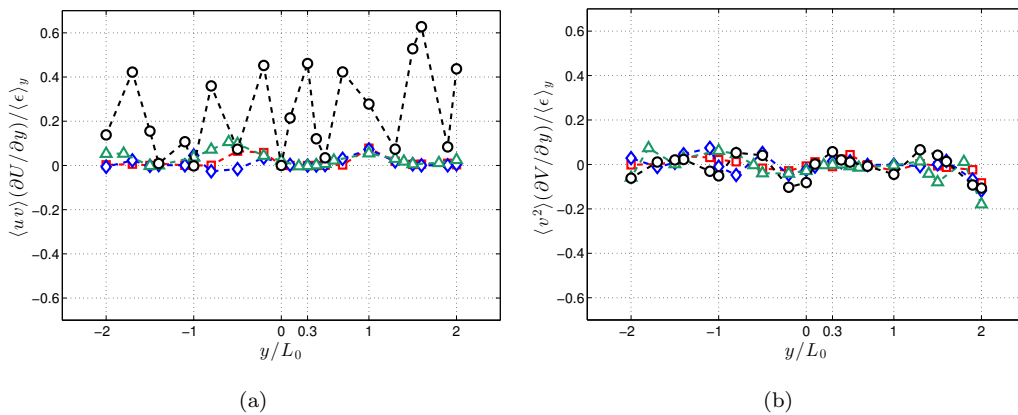
Figure 8.   Normalized profiles of the transverse production terms from (9); ($\bigcirc$) $x/L_0 = 10$, ($\square$) $x/L_0 = 25$, ($\diamondsuit$) $x/L_0 = 35$, ($\triangle$) $x/L_0 = 45$.

estimates of $\langle \epsilon \rangle_{XW}$ from (8) across a given transverse scan. Figure 8 demonstrates that production only has a significant presence near the grid. In particular, the primary production term is $\langle uv \rangle \, (\partial U/\partial y)$, which has peaks in the range of 40% to 60% of the dissipation. The $\langle v^2 \rangle \, (\partial V/\partial y)$ production term has a relatively negligible presence in both the near- and far-field. The presence of production due to non-zero transverse gradients near the grid is a contributing factor to the imbalance of (2) as production is not included in its derivation. Moreover the production is non-uniform, which further complicates the nature of the near-grid flow field.

We are also interested in $\partial(\langle vq^2 \rangle /2)/\partial y$ of the triple-correlation transport term, as it represents the transverse transport of turbulent kinetic energy by the turbulence itself. For convenience we define $\mathcal{T} = \langle vq^2 \rangle /2$. The presence of transverse transport was identified by Valente and Vassilicos [14] as a key difference between their fractal-generated turbulence and HIT. A non-zero transverse transport term, $\partial \mathcal{T}/\partial y \neq 0$, can be considered as a source of internal forcing.

Figures 9(a) and 9(b) show transverse scans at four streamwise locations of the triple-correlation, $\mathcal{T}$, and $\partial \mathcal{T}/\partial y$, respectively. From the figures, transverse transport of turbulent kinetic energy is negligible at the three streamwise positions in the homogeneous region, i.e. $x/L_0 = 25$, 35, and 45. However, the measurements conducted at $x/L_0 = 10$, within the inhomogeneous region, clearly demonstrate the existence of transverse transport of the turbulent kinetic energy there. The magnitude of the transverse transport term is comparable to the production term $\langle uv \rangle \, (\partial U/\partial y)$. The existence of transverse transport further suggests that (2) is not the appropriate equation for the energy budget in the near-field.

## 5.    Scaling range in the spectra and structure functions

The viscous term of (1) can be neglected in the inertial range such that (1) reduces to 'Kolmogorov's 4/5 law', $-\langle (\delta u)^3 \rangle = (4/5) \langle \epsilon \rangle r$, or equivalently, allowing for anisotropy [28],

$$-\langle (\delta u)(\delta q)^2 \rangle = \frac{4}{3} \langle \epsilon \rangle r. \tag{11}$$

Figure 10 shows the approach of $\langle (\delta u)(\delta q)^2 \rangle_n = -\langle (\delta u)(\delta q)^2 \rangle /(\langle \epsilon \rangle r)$ to 4/3. At $x/L_0 = 10.2$, $\langle (\delta u)(\delta q)^2 \rangle_n$ has a broad, flat peak with a maximum at 1.12, very near 4/3, while the peak of $\langle (\delta u)(\delta q)^2 \rangle_n$ and its flatness diminish with $x/L_0$. In the
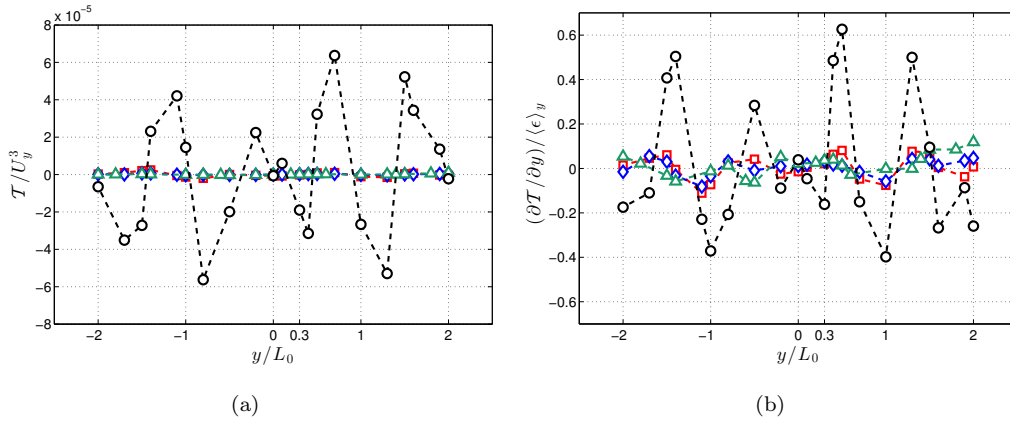
Figure 9.   Measurements of (a) the normalized transverse triple-correlation, and (b) the normalized turbulent transport of turbulent kinetic energy; $\mathcal{T} = \langle vq^2 \rangle /2$; ($\bigcirc$) $x/L_0 = 10$, ($\square$) $x/L_0 = 25$, ($\diamond$) $x/L_0 = 35$, ($\triangle$) $x/L_0 = 45$.
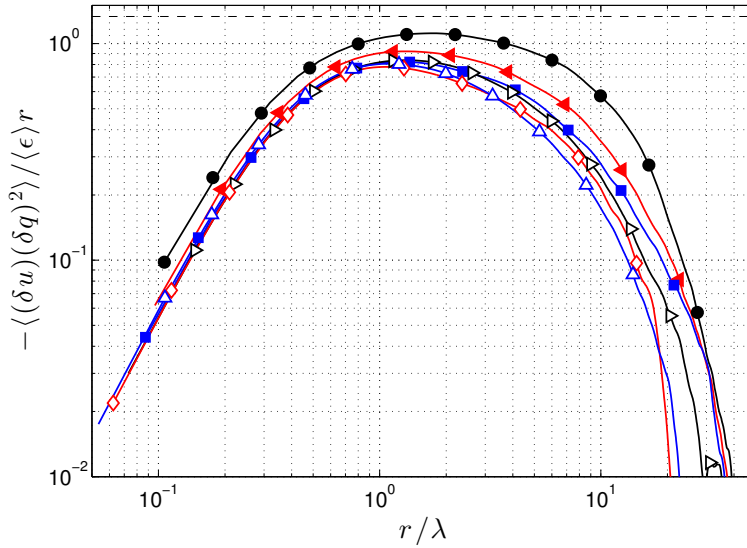


Figure 10.   Approach of $\langle (\delta u)(\delta q)^2 \rangle_n = -\langle (\delta u)(\delta q)^2 \rangle /(\langle \epsilon \rangle\, r)$ to 4/3 at several streamwise positions; ($\bullet$) $x/L_0 = 10.2$, $Re_\lambda = 138$; ($\blacktriangleleft$) $x/L_0 = 15.8$, $Re_\lambda = 106$; ($\blacksquare$) $x/L_0 = 20.0$, $Re_\lambda = 93$; ($\triangleright$) $x/L_0 = 27.3$, $Re_\lambda = 83$; ($\diamond$) $x/L_0 = 34.7$, $Re_\lambda = 80$; ($\triangle$) $x/L_0 = 42.4$, $Re_\lambda = 80$. Filled symbols represent data from the inhomogeneous region. Empty symbols represent data from the homogeneous region.

far-field, $\langle (\delta u)(\delta q)^2 \rangle_n$ becomes approximately self-similar, as demonstrated by the collapse at low $\tilde{r}$ in Figure 10. Evidently, the near-grid turbulence, which is likely forced by production and transverse transport of turbulent kinetic energy, produces $\langle (\delta u)(\delta q)^2 \rangle_n$ nearer to 4/3 at its peak than the decaying HIT in the far-field.

The shape of $\langle (\delta u)(\delta q)^2 \rangle_n$ and its approach to 4/3 are directly related to the existence of an inertial or scaling range. The presence of a scaling range can be considered in terms of the one-dimensional spectrum, $F_{11}$, defined here as, $\langle u^2 \rangle = \int_0^\infty F_{11}(k)\,\mathrm{d}k$. Figure 11 shows $F_{11}$ normalized by Kolmogorov variables at three downstream locations. In the near-grid region there is evidence of a scaling range that spans over a decade with an exponent near, but not exactly, $k^{-5/3}$. Earlier fractal studies have made similar observations [12–14]. At locations farther downstream, both the length of the scaling range and its slope decrease. Reynolds numbers for each curve are given in the captions to Figures 10 and 11. Comparison of the square-fractal-element grid-generated turbulence to classical grid-generated turbulence in the literature at similar $Re_\lambda$ (e.g. the 'regular' grid data acquired at
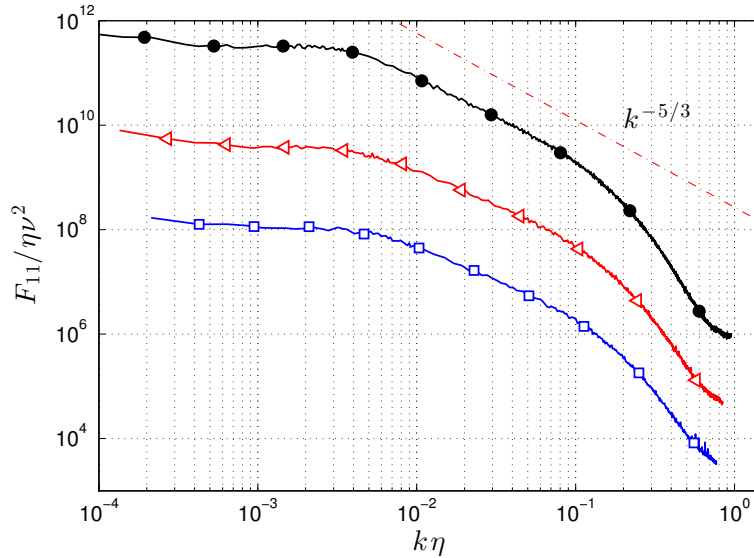
Figure 11.   One-dimensional spectra, $F_{11}$, normalized by Kolmogorov variables at several streamwise positions; ($\bullet$) $x/L_0 = 8.1$, $Re_\lambda = 154$; ($\triangleleft$) $x/L_0 = 24.2$, $Re_\lambda = 92$, offset by $10^{-1}$; ($\square$) $x/L_0 = 45.2$, $Re_\lambda = 80$, offset by $10^{-2}$.

$U = 20$ m/s in [14]) demonstrates that the onset of a clear scaling range occurs at lower $Re_\lambda$ for the present study. However, this feature of the turbulence is most prevalent in the region that does not approximate HIT and hence comparisons to theoretical predictions for HIT lose significance.

Antonia and Burattini [10] found that for a given $Re_\lambda$ there was a faster approach toward a scaling range for forced homogeneous turbulence compared to decaying homogeneous turbulence. A similar result is echoed here, that is the near-field results have a larger scaling range than classical grid experiments at similar $Re_\lambda$, as mentioned earlier. The primary difference between the aforementioned flows is inhomogeneity, however we suggest that perhaps this very inhomogeneity (which is characterized by the existence of non-uniform production and transport of turbulent kinetic energy) results in forcing, creating a scaling range that is more substantial in the forced near-field of a fractal grid compared to the unforced freely decaying region of a classical grid.

## 6.    Conclusions

Measurements behind a square-fractal-element grid have been investigated in the context of the scale-by-scale energy budget for grid turbulence as proposed by Danaila et al. [1]. It was found that in the far-field ($x/L_0 \geq 20$), where the flow is homogeneous, the scale-by-scale energy budget, described by (2), is well balanced. Furthermore, $-\langle (\delta u)(\delta q)^2 \rangle$ peaked near $r = \lambda$, which is consistent with previous classical grid-turbulence experiments and HIT simulations [7, 10, 11]. This provides further support to the argument of Hearst and Lavoie [18] that the far-fields of fractal-generated and classical grid-generated turbulence both exhibit Richardson-Kolmogorov phenomenology.

In the near-grid region ($x/L_0 < 20$), which overlaps with the region explored by previous fractal studies, it was shown that the scale-by-scale energy budget does not balance. In particular, there is a peak in the sum of the terms of the energy budget that represents an excess of energy, relative to the classical grid turbulence solution, for scales in the range $\lambda < r < L_0$. Furthermore, the peak of

$-\langle(\delta u)(\delta q)^2\rangle$ varied, and was located at $r > \lambda$. It was also identified that the near-grid region experiences non-zero transverse transport of turbulent kinetic energy and transverse $U$ and $V$ gradients, resulting in a non-zero production term. These forcing terms are expected to be the source of the imbalance in the near-grid scale-by-scale energy budget and differentiate the flow here from freely decaying HIT.

## Acknowledgements

## References

[1]   L. Danaila, F. Anselmet, and R.A. Antonia, *An overview of the effect of large-scale nonhomogeneities on small-scale turbulence*, Phys. Fluids 14 (2002), pp. 2475–2484.

[2]   A.N. Kolmogorov, *The Local Structure of Turbulence in Incompressible Viscous Fluids for Very Large Reynolds Numbers*, Dokl. Akad. Nauk SSSR 30 (1941), pp. 301–305.

[3]   A. Kolmogorov, *Dissipation of energy in the locally isotropic turbulence*, Dokl. Akad. Nauk SSSR 32 (1941).

[4]   K.R. Sreenivasan, *The passive scalar spectrum and the Obukhov-Corrsin constant*, Phys. Fluids 8 (1996), pp. 189–196.

[5]   L. Danaila, F. Anselmet, T. Zhou, and R.A. Antonia, *A generalization of Yaglom's equation which accounts for the large-scale forcing in heated decaying turbulence*, J. Fluid Mech. 391 (1999), pp. 359–372.

[6]   L. Danaila, F. Anselmet, and T. Zhou, *Turbulent energy scale-budget equations for nearly homogeneous sheared turbulence*, Flow Turb. Comb. 72 (2004), pp. 287–310.

[7]   P. Lavoie, P. Burattini, P. Djenidi, and R.A. Antonia, *Effect of initial conditions on decaying grid turbulence at low $R_\lambda$*, Exp. Fluids 39 (2005).

[8]   R.A. Antonia, R.J. Smalley, T. Zhou, F. Anselmet, and L. Danaila, *Similarity of energy structure functions in decaying homogeneous isotropic turbulence*, J. Fluid Mech. 487 (2003), pp. 245–269.

[9]   W.K. George, *The decay of homogeneous isotropic turbulence*, Phys. Fluids 4 (1992), pp. 1492–1509.

[10]  R.A. Antonia, and P. Burattini, *Approach to the 4/5 law in homogeneous isotropic turbulence*, J. Fluid Mech. 550 (2006), pp. 175–184.

[11]  P. Lavoie, L. Djenidi, and R.A. Antonia, *Effects of initial conditions in decaying turbulence generated by passive grids*, J. Fluid Mech. 585 (2007), pp. 395–420.

[12]  D. Hurst, and J.C. Vassilicos, *Scalings and decay of fractal-generated turbulence*, Phys. Fluids 19 (2007).

[13]  N. Mazellier, and J.C. Vassilicos, *Turbulence without Richardson-Kolmogorov cascade*, Phys. Fluids 22 (2010).

[14]  P.C. Valente, and J.C. Vassilicos, *The decay of turbulence generated by a class of multiscale grids*, J. Fluid Mech. 687 (2011), pp. 300–340.

[15]  P.C. Valente, and J.C. Vassilicos, *Universal Dissipation Scaling for Nonequilibrium Turbulence*, Phys. Rev. Lett. 108 (2012).

[16]  P.A. Krogstad, and P.A. Davidson, *Freely decaying, homogeneous turbulence generated by multi-scale grids*, J. Fluid Mech. 680 (2011), pp. 417–34.

[17]  P.A. Krogstad, and P.A. Davidson, *Near-field investigation of turbulence produced by multi-scale grids*, Phys. Fluids 24 (2012).

[18]  R.J. Hearst, and P. Lavoie, *Decay of turbulence generated by a square-fractal-element grid*, J. Fluid Mech. 741 (2014), pp. 567–584.

[19]  L.H. Benedict, and R.D. Gould, *Towards better uncertainty estimates for turbulence statistics*, Exp. Fluids 22 (1996), pp. 129–136.

[20]  J. Mi, R.C. Deo, and G.J. Nathan, *Fast-convergence iterative scheme for filtering velocity signals and finding Kolmogorov scales*, Phys. Rev. E 71 (2005).

[21]  J.C. Wyngaard, *Measurements of small-scale turbulence structure with hot wires*, J. Sci. Instr. 1 (1968), pp. 1105–1108.

[22]  Y. Zhu, and R.A. Antonia, *Effect of wire separation on X-probe measurements in a turbulent flow*, J. Fluid Mech. 287 (1995), pp. 199–223.

[23]  Y. Zhu, and R.A. Antonia, *The spatial resolution of hot-wire arrays for the measurement of small-scale turbulence*, Meas. Sci. Tech. 7 (1996), pp. 1349–1359.

[24]  R.J. Hearst, O.R.H. Buxton, B. Ganapathisubramani, and P. Lavoie, *Experimental estimation of fluctuating velocity and scalar gradients in turbulence*, Exp. Fluids 53 (2012), pp. 925–942.

[25]  R.A. Antonia, and P. Orlandi, *Similarity of decaying isotropic turbulence with a passive scalar*, J. Fluid Mech. 505 (2004).

[26]  S. Rajagopalan, R.A. Antonia, and L. Djenidi, *Effect of mesh grids on the turbulent mixing layer of an axisymmetric jet*, Heat Trans. Eng. 34 (2013), pp. 1216–1225.

[27]  S. Corrsin, *Turbulence: experimental methods*, in *Handbuch der Physik*, S. Flügge and C. Truesdell eds., Springer, 1963, pp. 524–89.

[28]  R.A. Antonia, M. Ould-Rouis, F. Anselmet, and Y. Zhu, *Analogy between predictions of Kolmogorov and Yaglom*, J. Fluid Mech. 332 (1997), pp. 395–409.